

## Supplementary Information

# Pt Single Atom and Atomic Cluster-Enhanced TiO<sub>2</sub> Janus Micromotors for Efficient Bubble Propulsion and Photocatalytic Environmental Remediation

Chang Lv,<sup>a</sup> Tao Wang,<sup>a</sup> Yeting Fang,<sup>a</sup> Yulong Ying,<sup>a</sup> Lvlv Ji,<sup>a</sup> Lei Liu <sup>\*b</sup>, and Sheng Wang <sup>\*a</sup>

<sup>a</sup>School of Materials Science and Engineering, Zhejiang Sci-Tech University, Hangzhou 310018, China

<sup>b</sup>Department of Physics, Zhejiang Sci-Tech University, Hangzhou 310018, China

### Corresponding Author

**Sheng Wang** ([wangsheng@zstu.edu.cn](mailto:wangsheng@zstu.edu.cn); [wangsheng571@hotmail.com](mailto:wangsheng571@hotmail.com))

**Lei Liu** ([leiliu@zstu.edu.cn](mailto:leiliu@zstu.edu.cn))

### List of Contents

<b>Section S1. Supplementary Notes</b>	<b>Page 2</b>
<b>Section S2. Supplementary Figures</b>	<b>Page 6</b>
<b>Section S3. Supplementary Tables</b>	<b>Page 17</b>
<b>Section S4. Supplementary Videos</b>	<b>Page 18</b>
<b>Section S5. Reference</b>	<b>Page 19</b>

---

## 1. Supplementary Notes

### S1.1 Principle of Electrospaying

During electrospaying process, a high electric potential applied to the stainless steel nozzle causes charge accumulation on the surface of the titanium sol, inducing electrostatic shear stress at the nozzle's outlet.<sup>1-3</sup> When the electrostatic forces exceed the solvent's surface tension, tiny primary droplets, or "mother droplets", are formed and ejected toward the collector (Supplementary Figure S12).<sup>4, 5</sup> Initially, these mother droplets maintain a spherical shape due to a uniform positive charge distribution balanced by surface tension. As the droplets travel, solvent evaporation causes charge migration to the extremities, resulting in an ellipsoidal shape due to mutual charge repulsion.<sup>6</sup> When the surface charge on a droplet exceeds the Rayleigh limit,<sup>7</sup> it further disintegrates into smaller "daughter droplets," which carry away some of the charge, allowing the remaining mother droplets to return to a spherical shape under surface tension.<sup>6</sup> Both mother and daughter droplets continue to evaporate and shrink during their trajectory, maintaining surface charge that prevents coalescence. For convenience, both droplet types are collectively referred to as micro-droplets in this study. As solvent evaporation proceeds, the increasing solute concentration within the micro-droplets initiates the solidification of titanium sol.

### S1.2 Péclet number

Péclet number ( $Pe$ ) characterizes the relative contributions of advection and diffusion to the motion of the colloids.<sup>8</sup> For evaporating spherical droplets,  $Pe$  is the ratio of the typical time, a dispersed particle needs to diffuse one initial droplet radius,  $\tau_d$ , and the characteristic time of evaporation,  $\tau_{ev}$ . For a (free) droplets, the evaporation time can be expressed as  $\tau_{ev} = R_0/v_{ev}$ , where  $R_0$  is the initial droplet radius and  $v_{ev}$  is the speed of the receding liquid-air interface. For a free micro-droplet, evaporation is limited by the diffusion of solvent molecules through the surrounding air,<sup>9</sup> and the micro-droplet volume  $V$  decreases as:

$$V^{\frac{2}{3}} = V_0^{\frac{2}{3}} - \alpha t \quad \text{S1}$$

where  $V_0$  is the initial volume of the micro-droplet and  $\alpha$  is the rate of surface reduction. Taking the time derivative of Equation S1, the initial  $v_{ev}$  can be expressed as:

$$v_{ev} = \frac{1}{2} \left( \frac{3}{4\pi} \right)^{\frac{2}{3}} \frac{\alpha}{R_0} \quad \text{S2}$$

For a free and spherical micro-droplet,  $\alpha$  can be determined analytically as:<sup>8</sup>

$$\alpha_{\text{free}} = 2 \left( \frac{4\pi}{3} \right)^{\frac{2}{3}} \frac{D_{\text{air}} m \Delta P}{\rho k_B T} \quad \text{S3}$$

Here,  $D_{\text{air}}$  is the diffusion coefficient of vapor molecules in air,  $m$  is the mass of one vapor/liquid molecule,  $\rho$  is the density of the liquid,  $\Delta P$  is the difference in pressure at the droplet surface and outside the film of vapor, and  $k_B T$  is the thermal energy of the system. The pressure difference  $\Delta P$  in Equation S4 can be expressed in terms of relative humidity  $RH$  as  $\Delta P = (1 - RH)P_s$  with saturation vapor pressure  $P_s$ .

The characteristic diffusion time can be expressed as:<sup>8</sup>

$$\tau_d = \frac{R_0^2}{D_p} \quad \text{S4}$$

where  $D_p$  is the diffusion coefficient of the sol, which can be estimated through the Stokes–Einstein relation,  $D_p = k_B T / (3\pi\eta d)$ , with suspension viscosity  $\eta$ . For dilute suspensions of spherical particles, Cichocki and Felderhof showed that  $\eta$  can be estimated within reasonable accuracy using  $\eta = \eta_s (1 + 2.5\phi + 5.913\phi^2)$ , with solvent viscosity  $\eta_s$ .<sup>10</sup> This expression can be considered a correction of order  $\phi^2$  to the Einstein viscosity equation.<sup>11, 12</sup>

As a result, for evaporating free and spherical micro-droplets,  $Pe$  can be expressed as:

$$Pe = \frac{\tau_d}{\tau_{\text{ev}}} = \frac{1}{2} \left( \frac{3}{4\pi} \right)^{\frac{2}{3}} \frac{\alpha_{\text{free}}}{D_p} \quad \text{S5}$$

which is independent of the initial micro-droplet radius. It should be noted that the  $Pe$  values quoted in this work refer to the beginning of the evaporation process when the micro-droplets still have their initial radius  $R_0$ . As the droplet dries, the local solute volume fraction increases, resulting in a local increase in micro-droplets viscosity. Consequently,  $Pe$  increases over time and eventually becomes undefined once the solutes solidify or crystallize. Nevertheless, the initial  $Pe$  values are useful for characterizing the drying regime of the micro-droplets.

### S1.3 Self-assembly of Janus micro-bowls

The self-assembly of Janus micro-bowls is primarily governed by the solvent evaporation rate. As described in prior literature,<sup>8, 13</sup> the evaporation rate of a free droplet is diffusion-limited and follows the relationship:

$$V^{2/3} = V_0^{2/3} - \alpha_R t \quad \text{S6}$$

Here,  $V_0$  is the initial droplet volume,  $\alpha_R$  is the evaporation rate,  $t$  is the evaporation time, which can be expressed as  $t = R_0/v_r$ , where  $R_0$  is the initial droplet radius and  $v_r$  is the receding speed of the droplet-air interface.

---

In the electro spraying process, the size and volume of the generated droplets are strongly influenced by electric field strength (applied voltage) and liquid injection rate.<sup>14</sup> The effects of applied voltage were observed in the electro spraying of titanium sol (Supplementary Figures S16–S17).

At lower applied voltages (e.g., 10 kV), the charge density on the droplet surface does not reach the Rayleigh limit,<sup>6, 7</sup> preventing droplet fission. This results in larger droplet volumes, where incomplete solvent evaporation during jetting leads to heterogeneous morphologies. This observation aligns with previous studies, such as the report by Notz and Basaran, which demonstrated that droplet volume decreases linearly with increasing Bond number.<sup>3</sup> Additionally, achieving uniform droplet sizes under a direct current electric field remains challenging, contributing to the inhomogeneous size of Janus micro-bowls.<sup>14</sup>

To further optimize electro spraying parameters, we adjusted the flow rate and nozzle-to-collector distance at an optimal applied voltage (Supplementary Figures S18–S19). Three distinct deposition morphologies of titanium sol were observed:

1. **Unformed:** Titanium sol is deposited directly in a liquid state, with solvent volatilization occurring on the receiver.
2. **Partially formed:** A fraction of titanium sol assembles into Janus micro-bowls, while others remain in the solution state.
3. **Fully formed:** Titanium sol is completely assembled into Janus micro-bowls.

These morphologies are closely related to the efficiency of desolvation during the electro spraying process.

#### S1.4 DRIFTS measurements

The diffuse reflectance infrared Fourier transform spectroscopy (DRIFTS) analysis with CO as the probe molecule is performed on a Bruker TENSOR II FTIR spectrometer equipped with a mercury-cadmium-tellurium (MCT) detector cooled by liquid nitrogen. Prior to each analysis, the sample is placed in the test chamber and pretreated at 423 K in Ar atmosphere for 30 min. After cooling to room temperature, the background spectrum is acquired from 4000 to 400  $\text{cm}^{-1}$ . Subsequently, the sample is exposed in a mixed CO/Ar (10 vol% CO and 90 vol% Ar) atmosphere for 30 min to achieve the adsorption equilibrium of CO, followed by blowing pure Ar gas to purge the physically adsorbed CO molecules. The CO-DRIFTS spectra are collected after the gas is turned to pure Ar for 15 min.

In situ DRIFTS analysis for photocatalytic selective oxidation of benzylamine in the presence of a little water is also carried out on the Bruker TENSOR II FTIR spectrometer. Specifically, 30 mg of the photocatalyst is placed on the sample holder in the test chamber and 100  $\mu\text{L}$  of the mixture (500  $\mu\text{L}$  H<sub>2</sub>O and 500  $\mu\text{L}$  benzylamine) was injected into the chamber.

---

After the chamber is purged with Ar gas for 30 min, the background spectrum is recorded from 4000 to 400  $\text{cm}^{-1}$ . Subsequently, the test chamber is heated to 423 K for 30 min to achieve that the benzylamine and  $\text{H}_2\text{O}$  molecules are volatilized and adsorbed on the photocatalyst. After the excess vapor of benzylamine and  $\text{H}_2\text{O}$  is purged by Ar gas, the time-dependent DRIFTS spectra are recorded to monitor the photocatalytic selective oxidation of benzylamine under the irradiation of Xe lamp.

## S2. Supplementary Figures

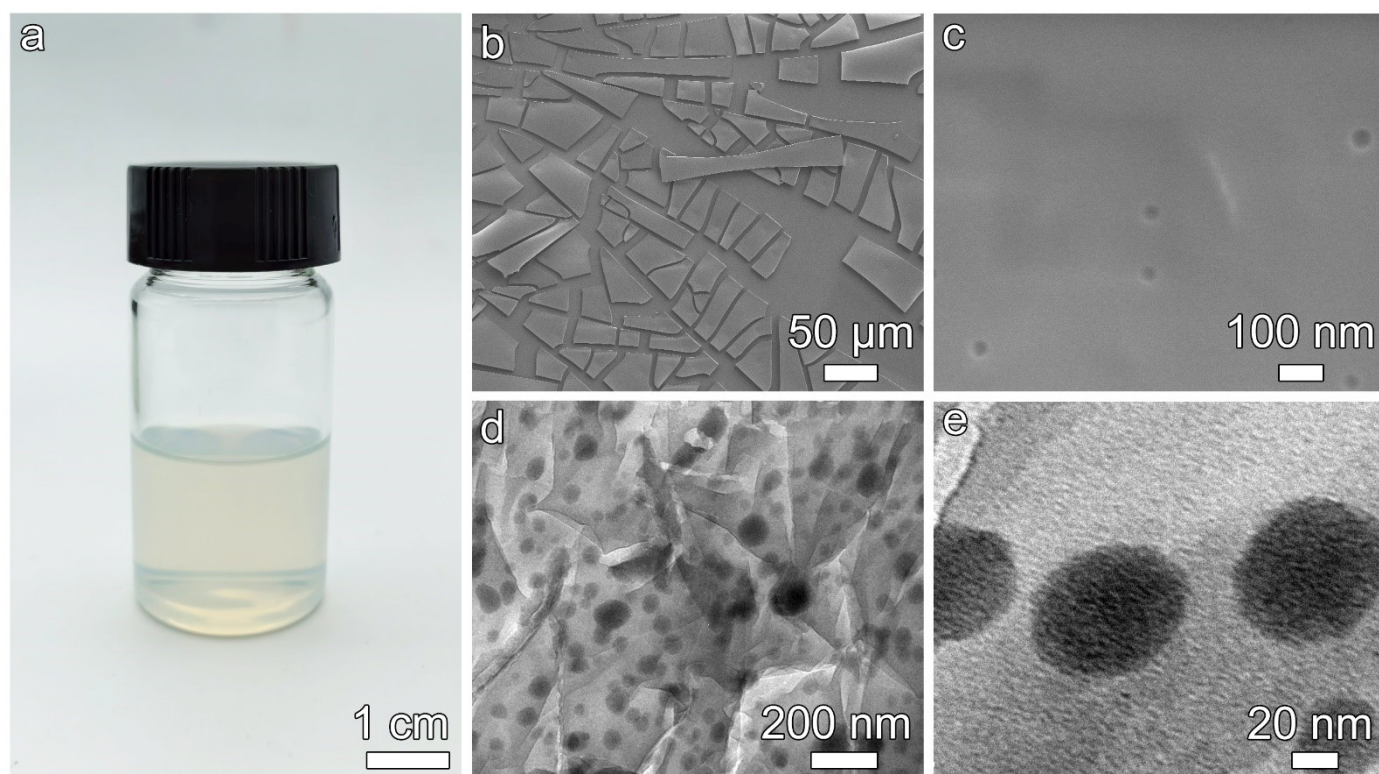


**Figure S1. Characteristic of titanium sol.** (a) Photograph of the titanium sol used in this study, displaying a stable, negatively charged colloidal system with no visible settling or aggregation over several months. (b, c) SEM and (d, e) TEM images of the titanium sol shown in (a), illustrating its structural properties.

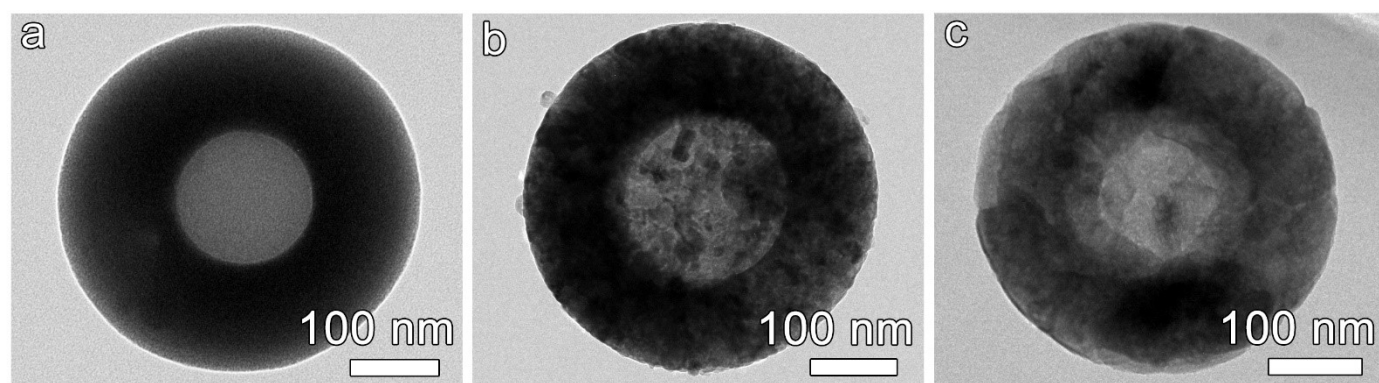


**Figure S2. TEM Images of micro-bowl variants.** (a) Amorphous  $\text{TiO}_2$  micro-bowls, (b) anatase  $\text{TiO}_2$  micro-bowls, and (c) anatase  $\text{TiO}_2\text{-V}_\text{o}$  micro-bowls.

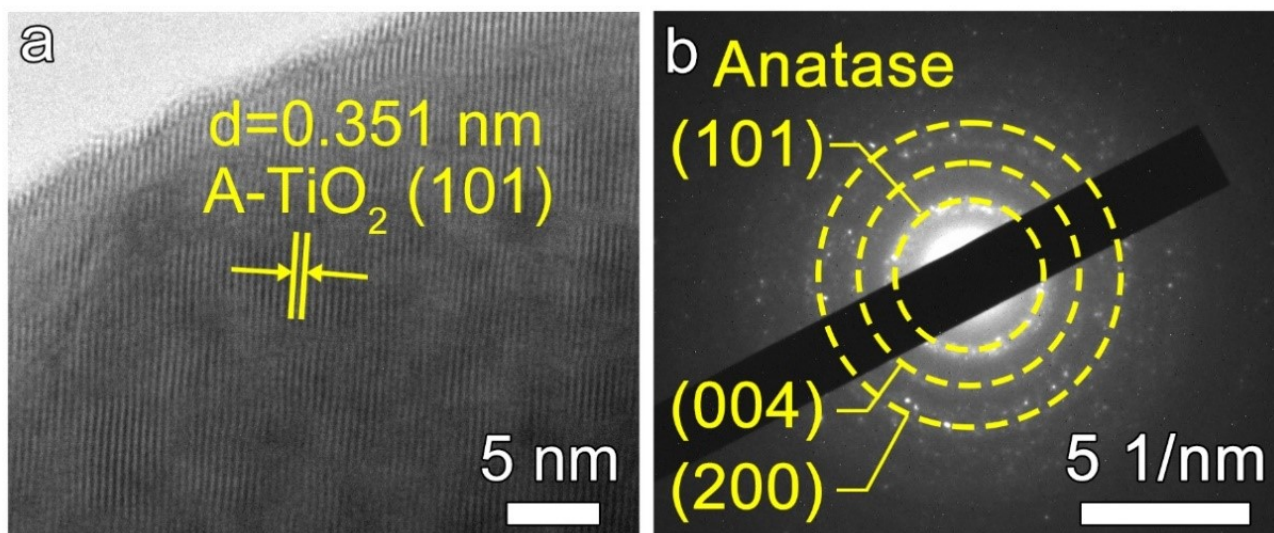


**Figure S3. Characterization of anatase TiO<sub>2</sub> micro-bowls.** (a) HRTEM image and (b) SAED pattern of anatase TiO<sub>2</sub> micro-bowls.

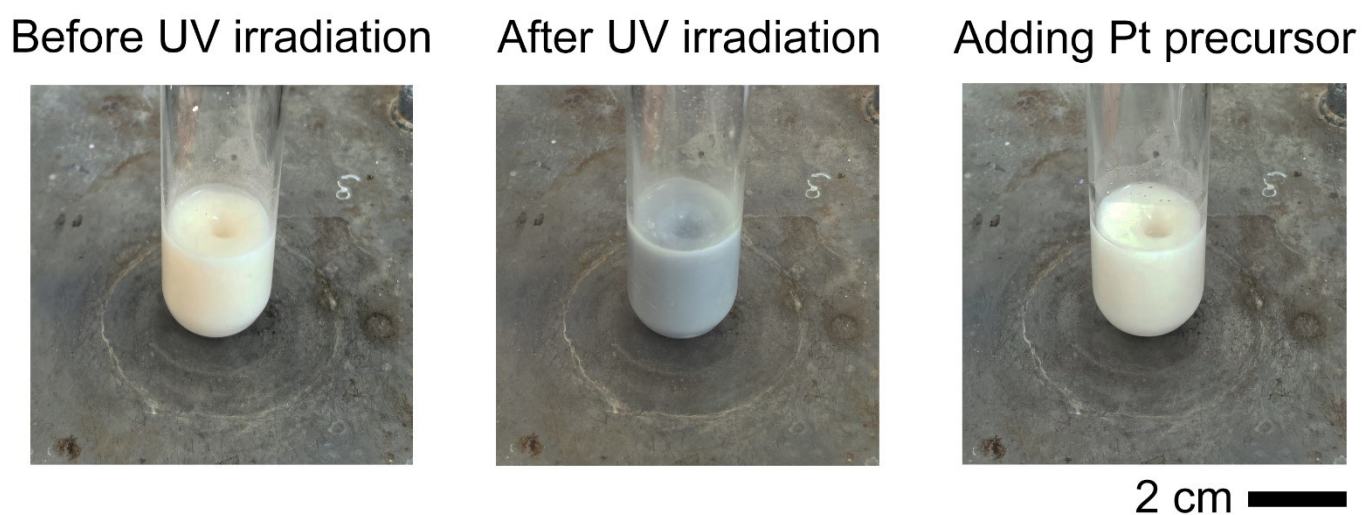


**Figure S4. Schematic and photographs of Pt<sub>SA&C</sub>-TiO<sub>2</sub> Janus micromotor synthesis.** Illustration of the synthesis process of Pt<sub>SA&C</sub>-TiO<sub>2</sub> Janus micromotors via photochemical defect tuning strategy.

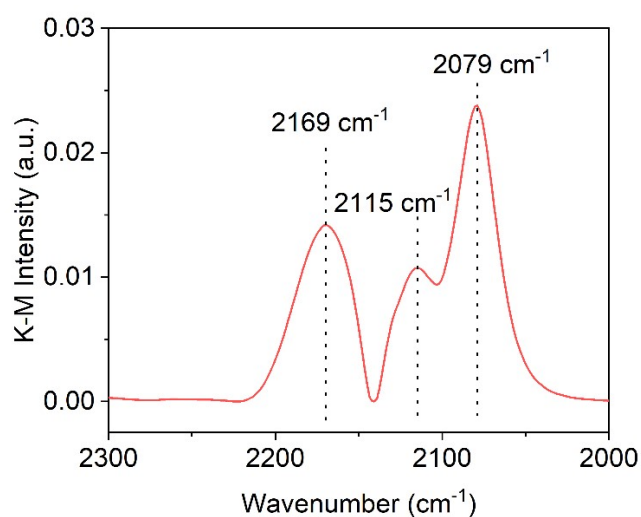


**Figure S5. Spectral characterization of Pt<sub>SA&C</sub>-TiO<sub>2</sub> Janus micromotor.** CO-DRIFTS spectra of Pt<sub>SA&C</sub>-TiO<sub>2</sub> Janus micromotor.

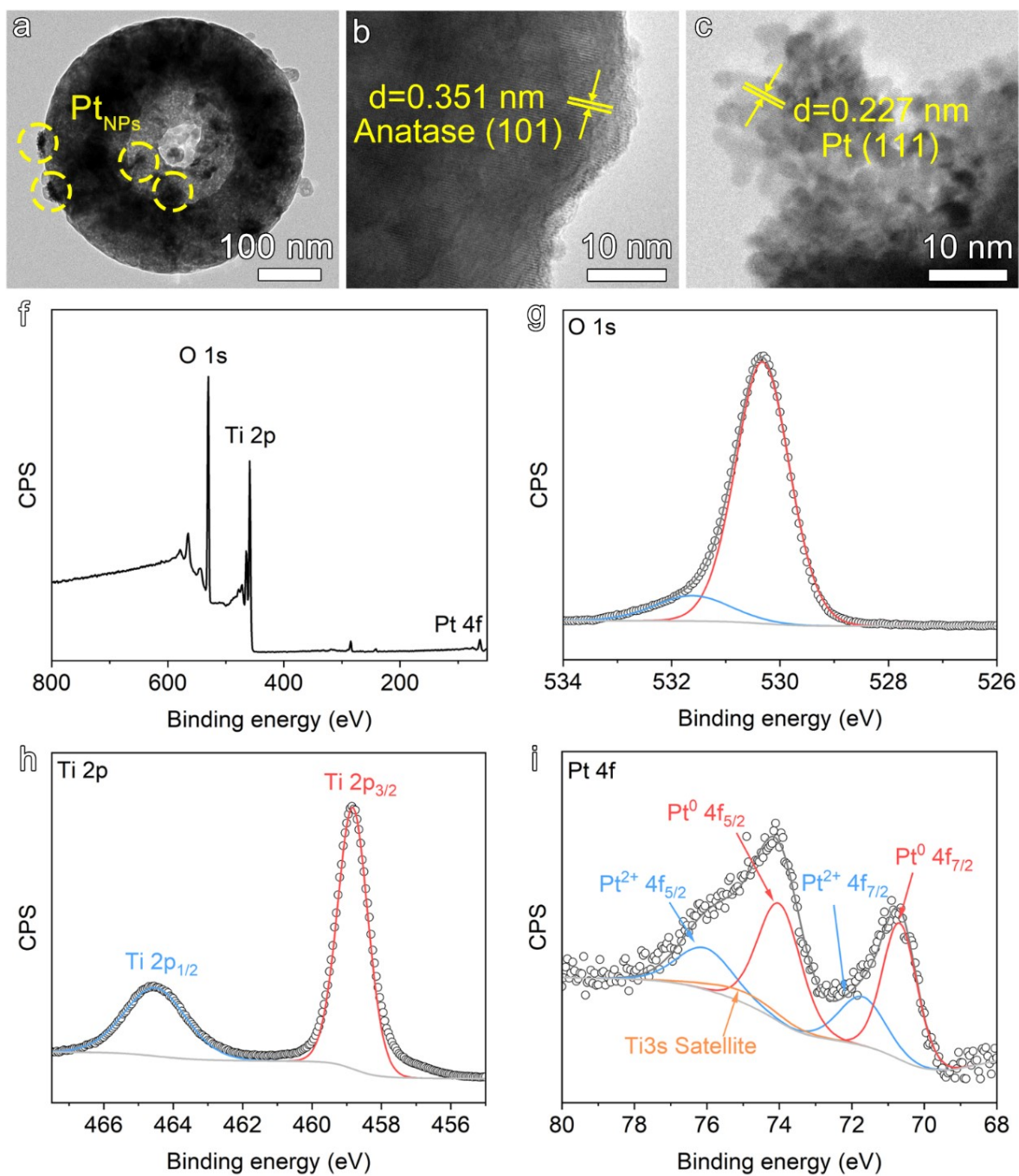


**Figure S6. Characterization of Pt<sub>NPs</sub>-TiO<sub>2</sub>.** (a) TEM images of Pt<sub>NPs</sub>-TiO<sub>2</sub>. (b, c) HRTEM images showing anatase TiO<sub>2</sub> with lattice fringe of 0.351 nm (101 facet) and Pt NPs with lattice fringe of 0.227 nm (111 facet). (d-f) XPS spectra for Pt 4f, Ti 2p, and O 1s of Pt<sub>NPs</sub>-TiO<sub>2</sub>. High-resolution Pt 4f analysis shows Pt in multiple oxidation states, with Pt 4f<sub>7/2</sub> peaks at 70.7 eV (Pt<sup>0</sup>) and 71.8 eV (Pt<sup>2+</sup>) and Pt 4f<sub>5/2</sub> peaks at 74.1 and 76.2 eV, confirming Pt-Pt bonding and successful Pt NPs decoration.

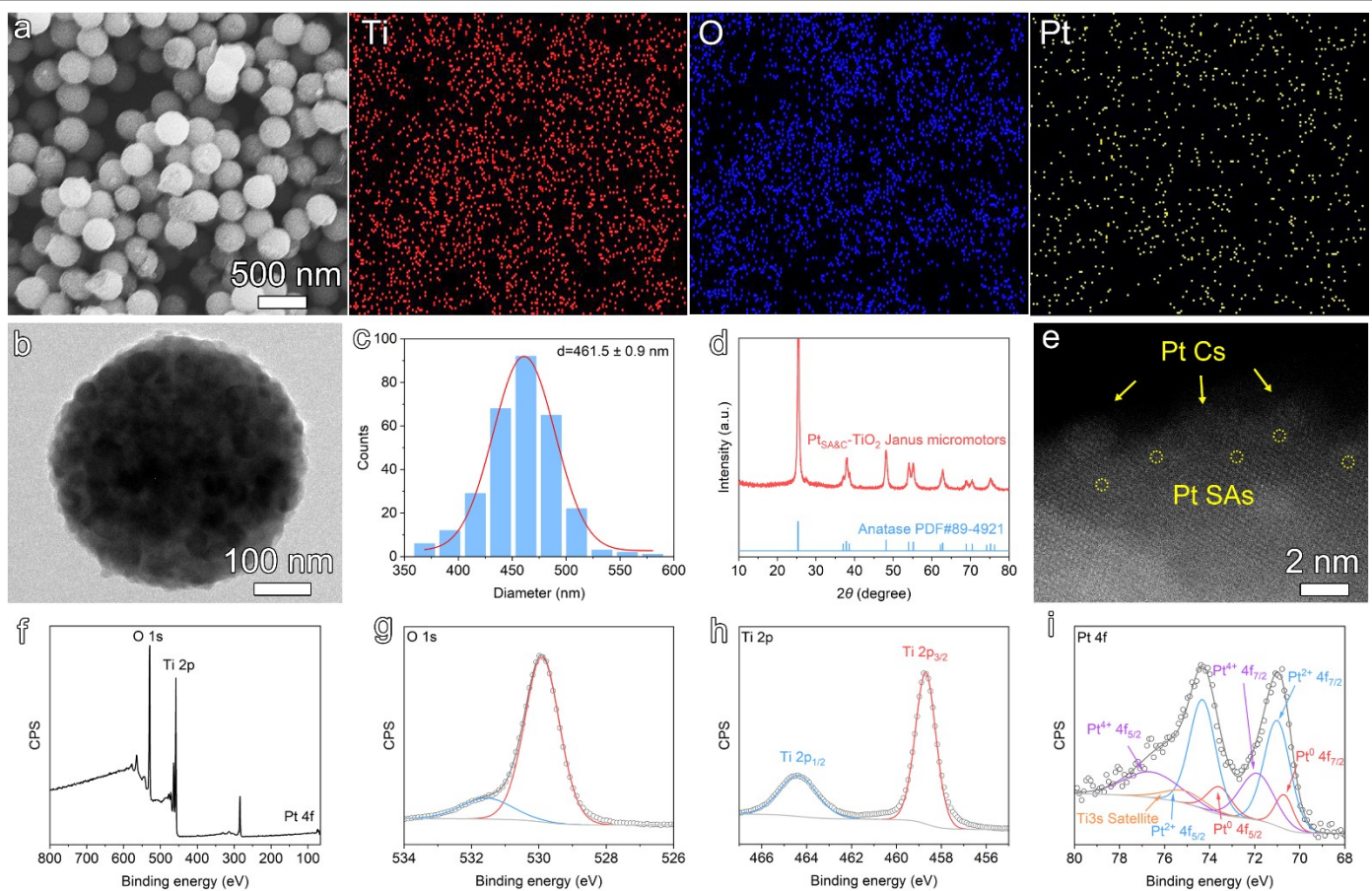


**Figure S7. Characterization of Pt<sub>SA&C</sub>-TiO<sub>2</sub> microspheres.** (a) SEM image and SEM-EDS elemental mapping of Pt<sub>SA&C</sub>-TiO<sub>2</sub> microspheres. (b) TEM image of TiO<sub>2</sub> microspheres. (c) Particle size distribution (average diameter: 461.5 ± 0.9 nm) based on 300 randomly selected micromotors. (d) XRD patterns of Pt<sub>SA&C</sub>-TiO<sub>2</sub> microspheres. (e) Cs-STEM image of Pt<sub>SA&C</sub>-TiO<sub>2</sub> microspheres. (f-i) XPS spectra of Pt 4f, Ti 2p, and O 1s for Pt<sub>SA&C</sub>-TiO<sub>2</sub> microspheres.

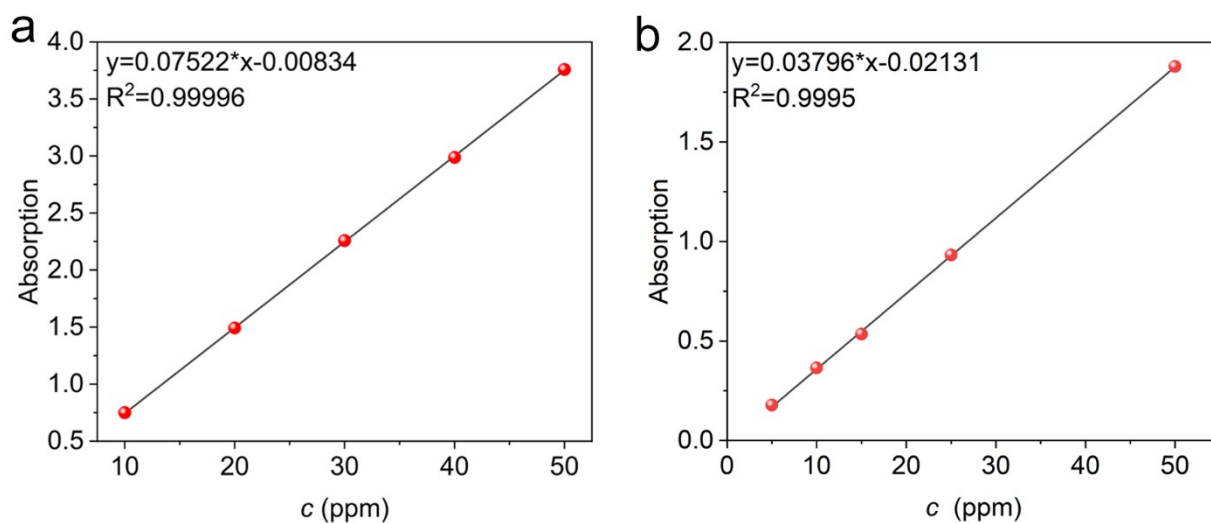


**Figure S8. Standard calibration curves.** Absorbance-concentration calibration curve (a) for methyl orange (MO) and (b) for tetracycline hydrochloride (TCH).

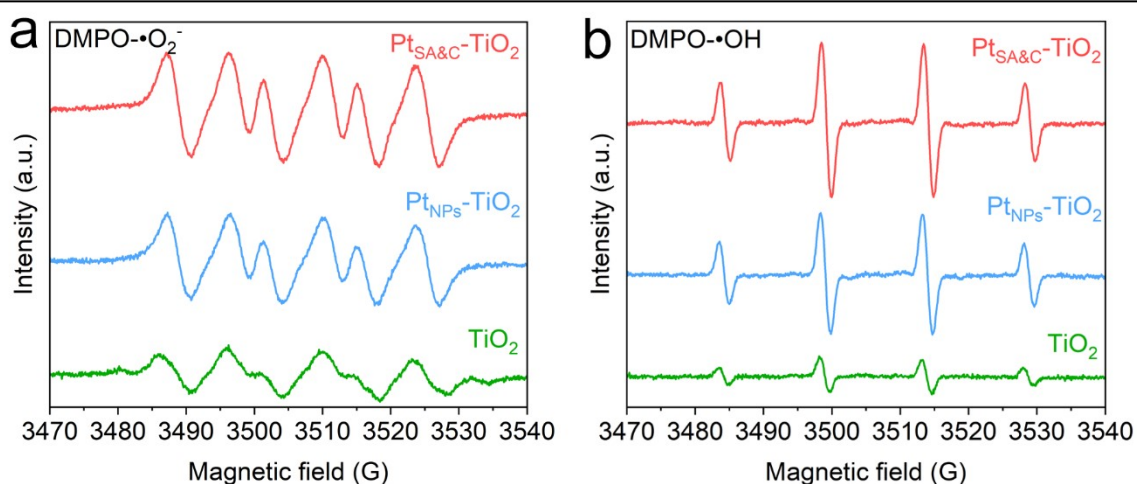


**Figure S9. EPR Spectra for Radical Detection.** Electron paramagnetic resonance (EPR) spectra of DMPO- $\bullet\text{O}_2^-$  and DMPO- $\bullet\text{OH}$  for anatase  $\text{TiO}_2$  micro-bowls (green),  $\text{Pt}_{\text{NPs}}\text{-TiO}_2$  Janus micromotors (blue), and  $\text{Pt}_{\text{SA\&C}}\text{-TiO}_2$  Janus micromotors (red) after simulated solar irradiation.

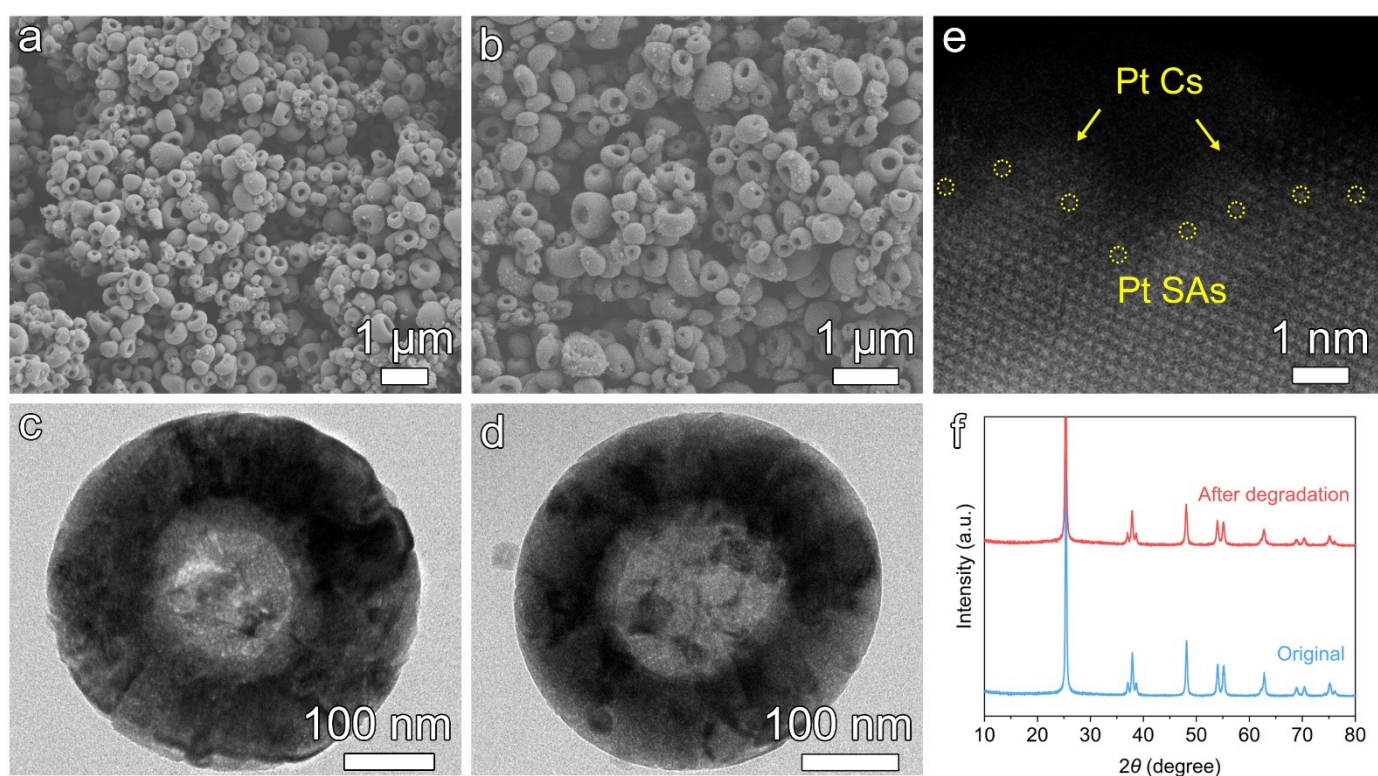


**Figure S10. Characteristics of  $\text{Pt}_{\text{SA\&C}}\text{-TiO}_2$  Janus micromotors before and after photodegradation.** (a, c) SEM and TEM images of  $\text{Pt}_{\text{SA\&C}}\text{-TiO}_2$  Janus micromotors before degradation, and (b, d) SEM and TEM images after degradation. (e) Cs-STEM image of  $\text{Pt}_{\text{SA\&C}}\text{-TiO}_2$  Janus micromotors after photodegradation. (f) XRD patterns comparing  $\text{Pt}_{\text{SA\&C}}\text{-TiO}_2$  Janus micromotors before and after photodegradation.

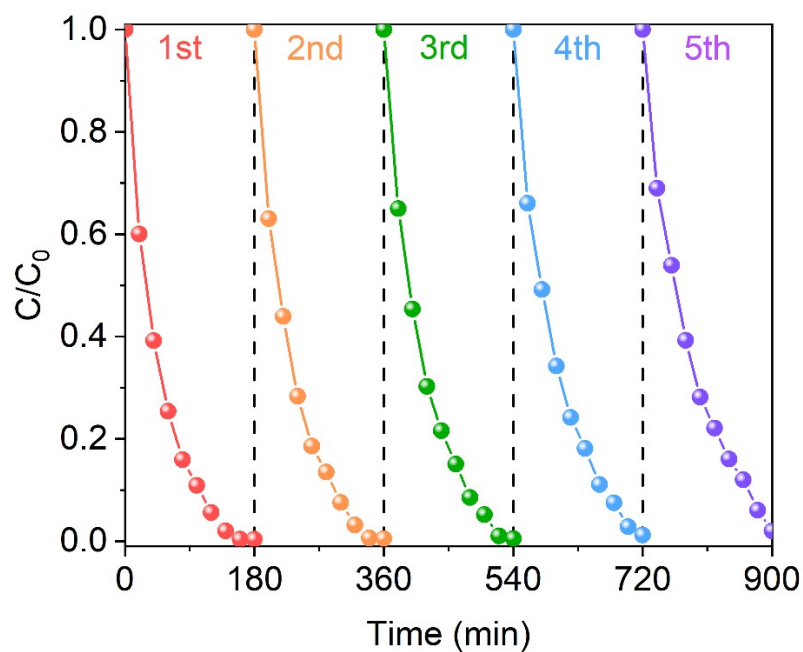


**Figure S11.** Reusability of Pt<sub>SA&C</sub>-TiO<sub>2</sub> Janus micromotors in the photodegradation of TCH.

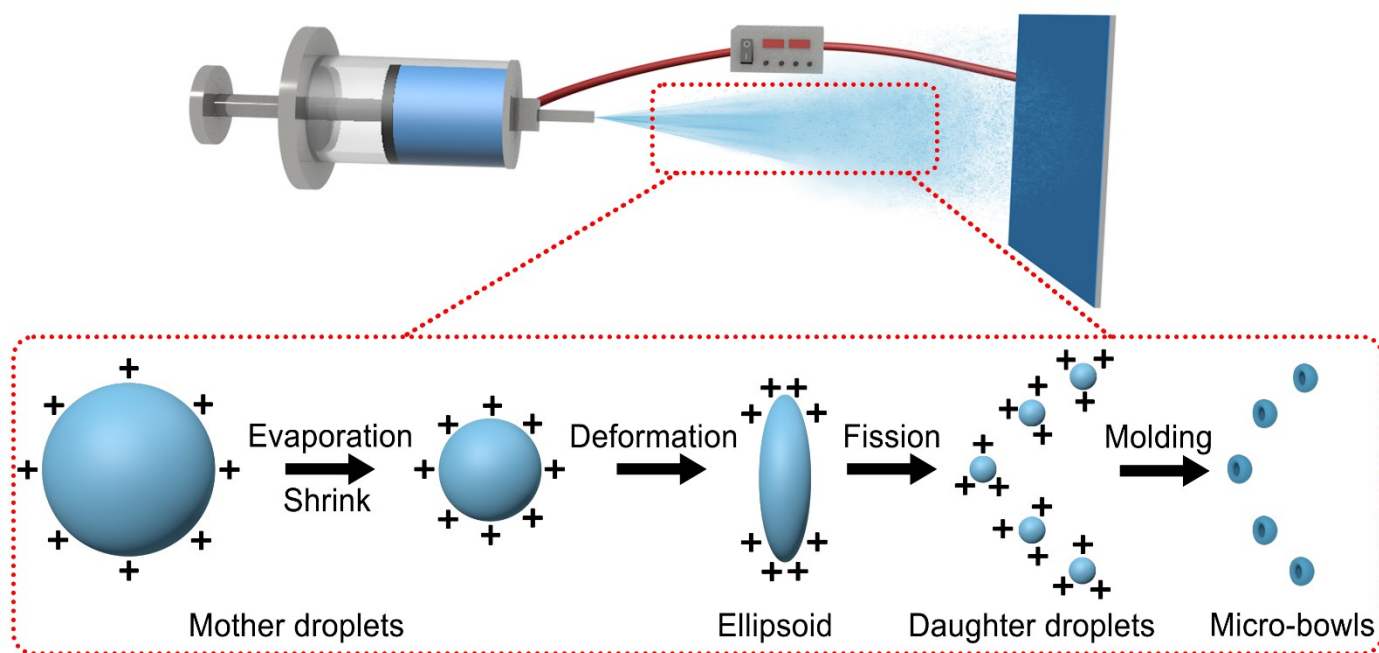


**Figure S12. Fabrication of Janus micro-bowls via electrospaying.** Schematic representation of the self-assembly process for constructing Janus micro-bowls from titanium sol using the electrospaying technique.

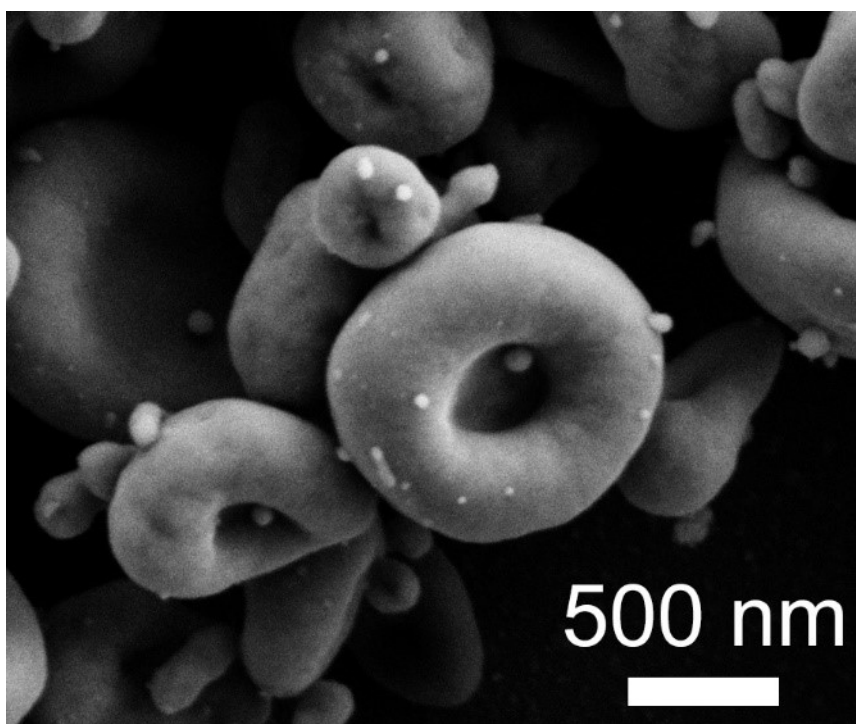


Figure S13. SEM image of electrospayed micro-products at 30 °C.

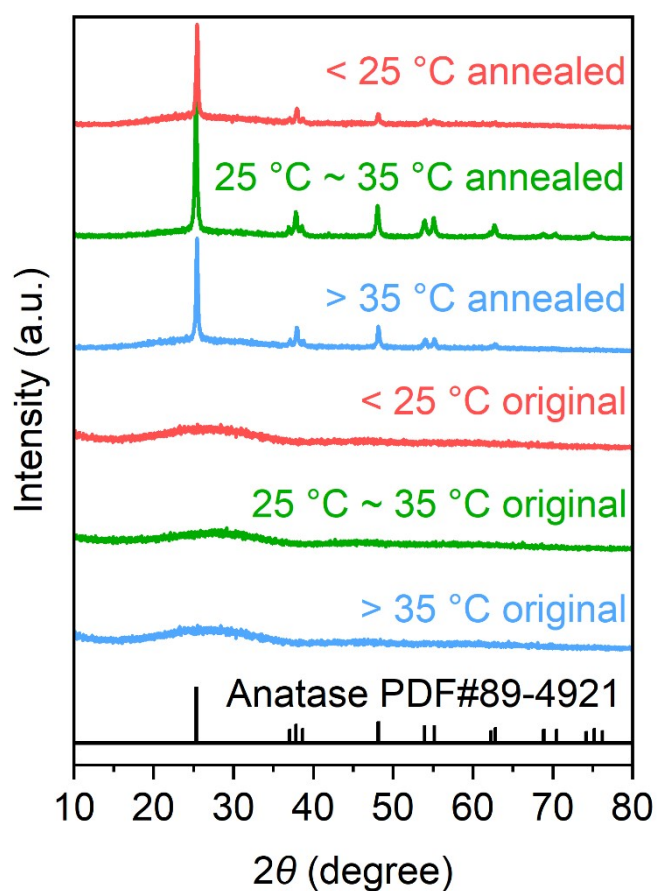
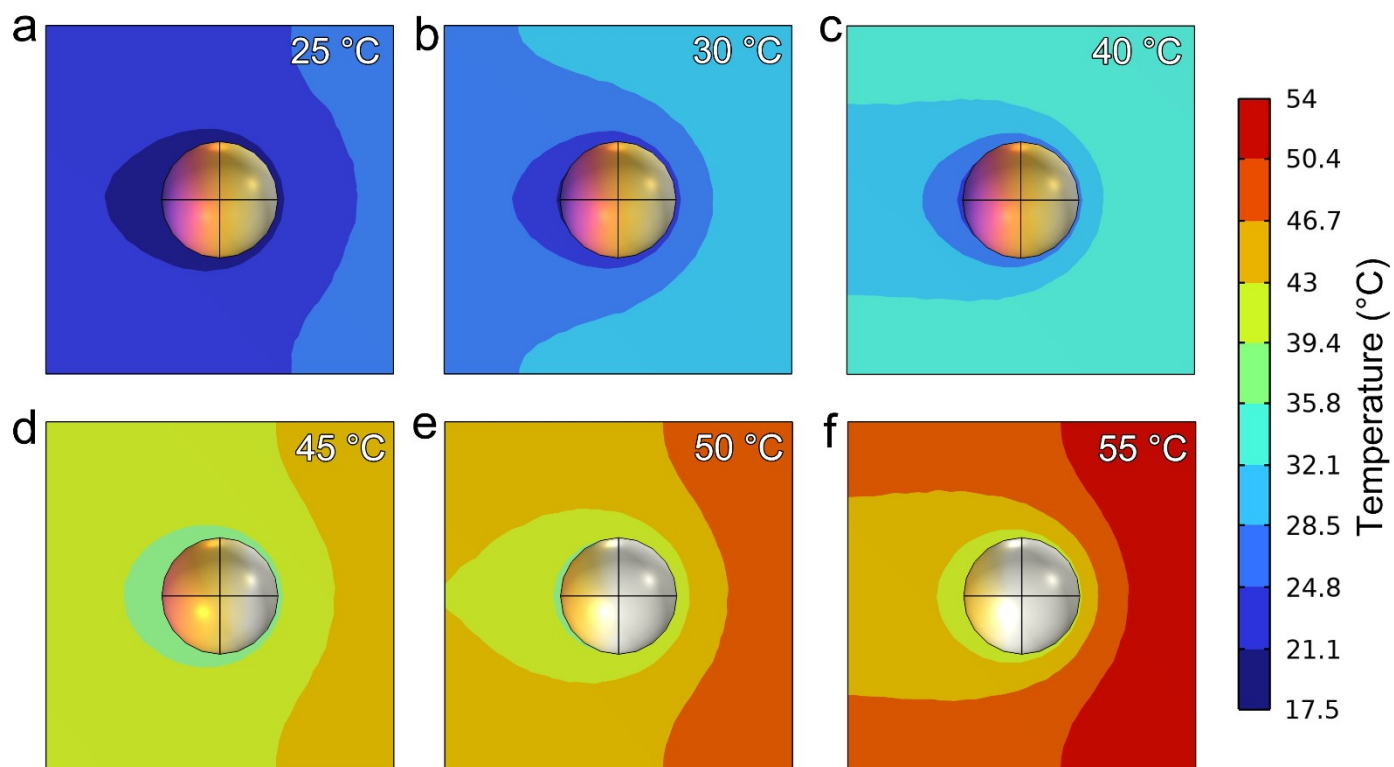
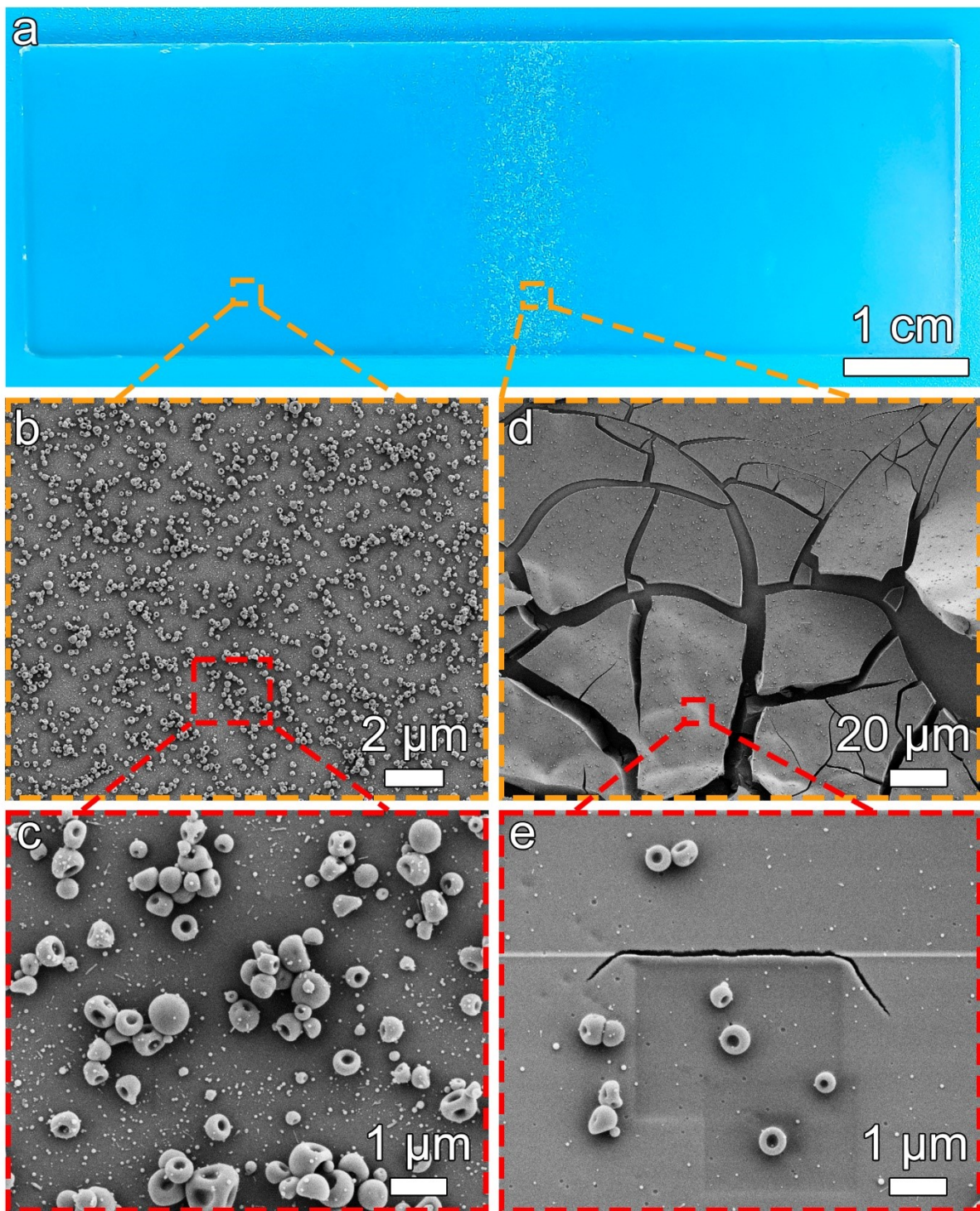


Figure S14. Temperature influence on the fabrication of Janus micro-bowls and post-calcination analysis. XRD patterns of micro-products fabricated at varying temperatures: < 25 °C (red), 25–35 °C (green), and > 35 °C (blue), and their respective post-calcination samples, showing structural changes before and after calcination.



**Figure S15. Simulated temperature difference of micro-droplets.** Simulated temperature distributions in micro-droplets at ambient temperatures of (a) 25 °C, (b) 30 °C, (c) 40 °C, (d) 45 °C, (e) 50 °C, and (f) 55 °C, respectively.



**Figure S16. Electrospaying deposition on glass slide at 10 kV** (a) Digital image of a glass slide following electrospaying at an applied voltage of 10 kV. (b–c) SEM images of the thin-coated side of the glass slide. (d–e) SEM images of the thick-coated side, showing incomplete desolventing of large droplets, resulting in direct deposition of titanium sol and a visible white central area on the slide.

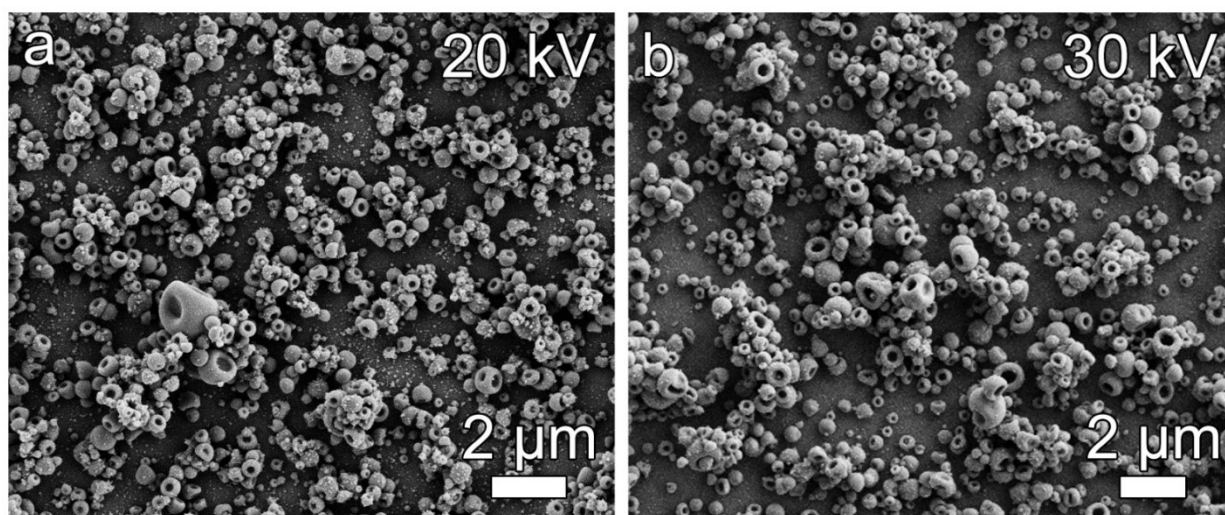


**Figure S17. Surface morphology at different electro spraying voltages.** SEM images showing variations in surface morphology after electro spraying at applied voltages of (a) 20 kV and (b) 30 kV.

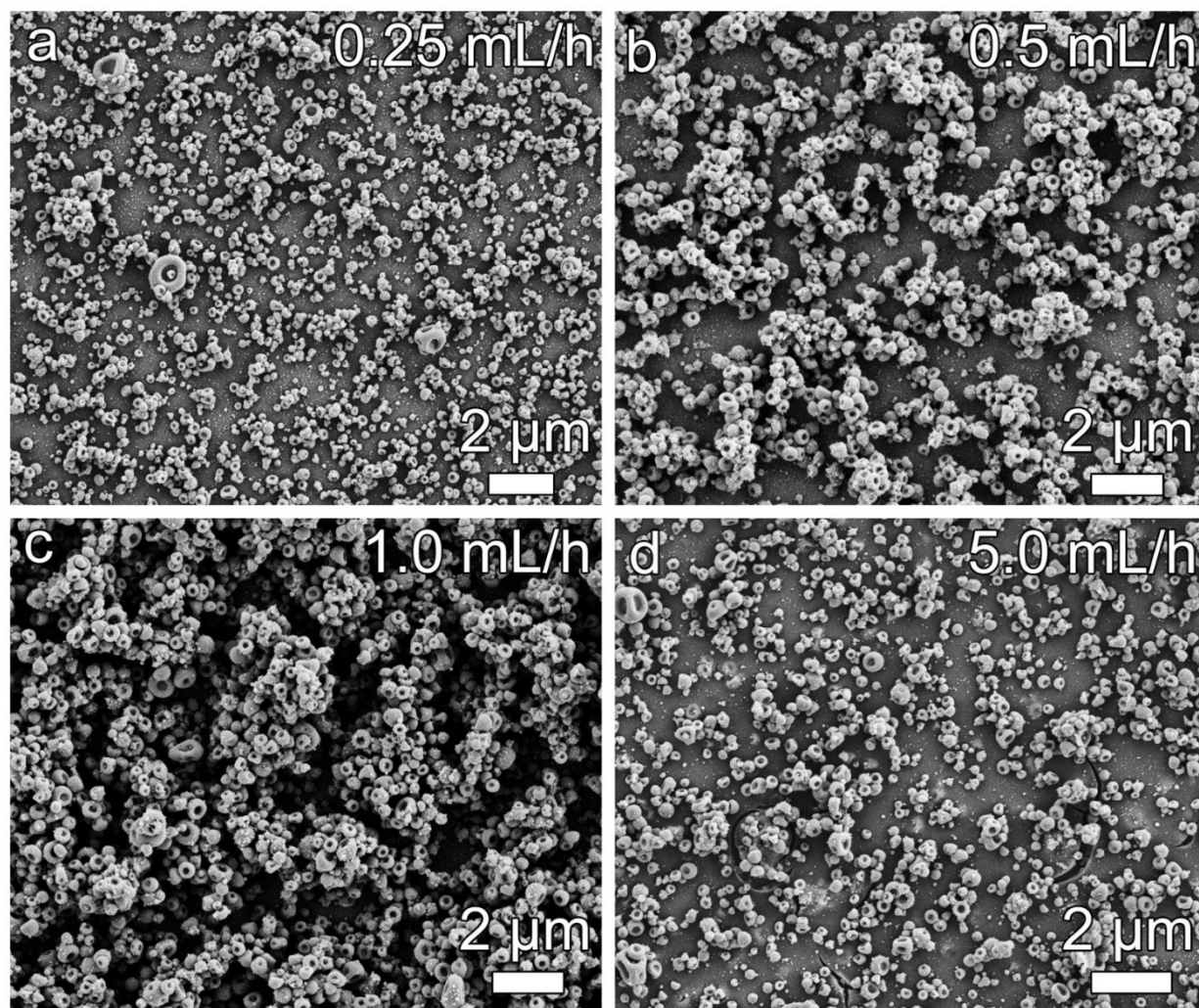


**Figure S18. Surface morphology at 20 kV with varying flow rates.** SEM images showing surface morphology variations after electro spraying at a constant voltage of 20 kV with different flow rates: (a) 0.25 mL/h, (b) 0.5 mL/h, (c) 1.0 mL/h, and (d) 5.0 mL/h.

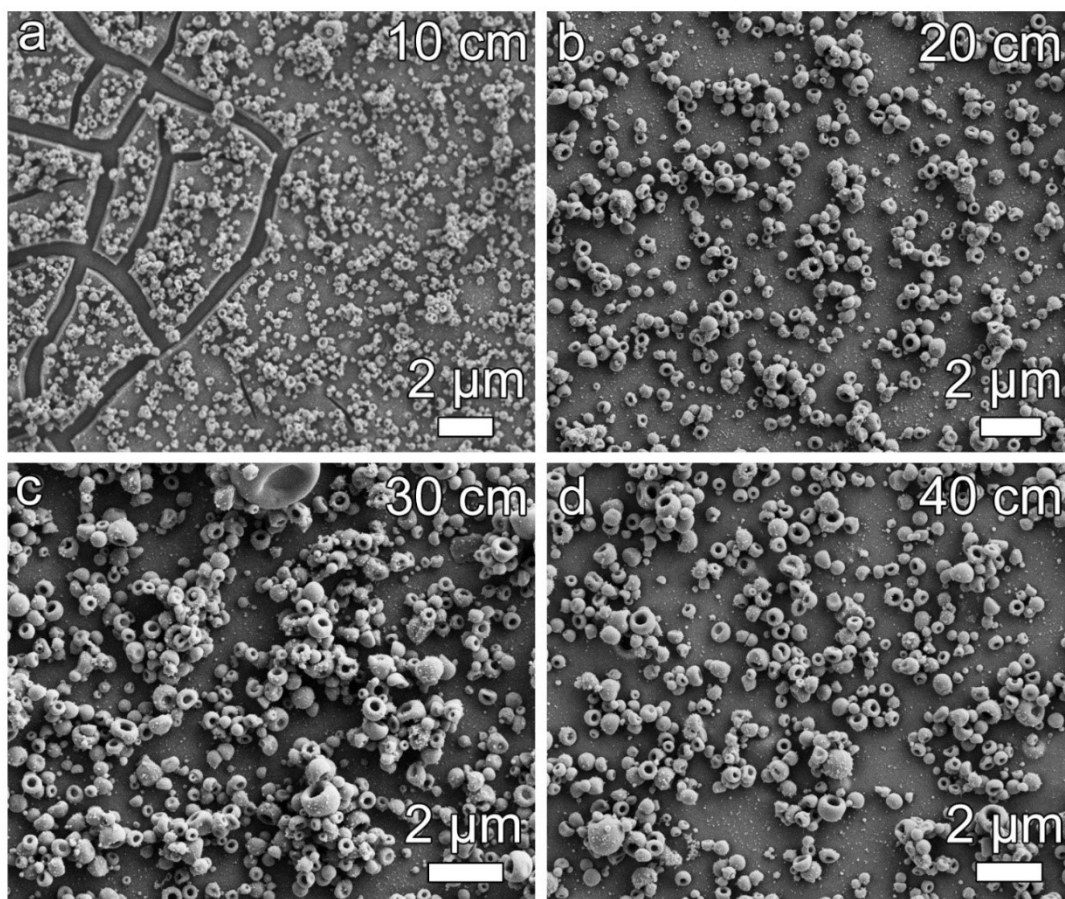


**Figure S19. Surface morphology at 20 kV with varying Nozzle-to-Collector distances.** SEM images showing surface morphology variations after electrospaying at a constant voltage of 20 kV with different nozzle-to-collector distances: (a) 10 cm, (b) 20 cm, (c) 30 cm, and (d) 40 cm.

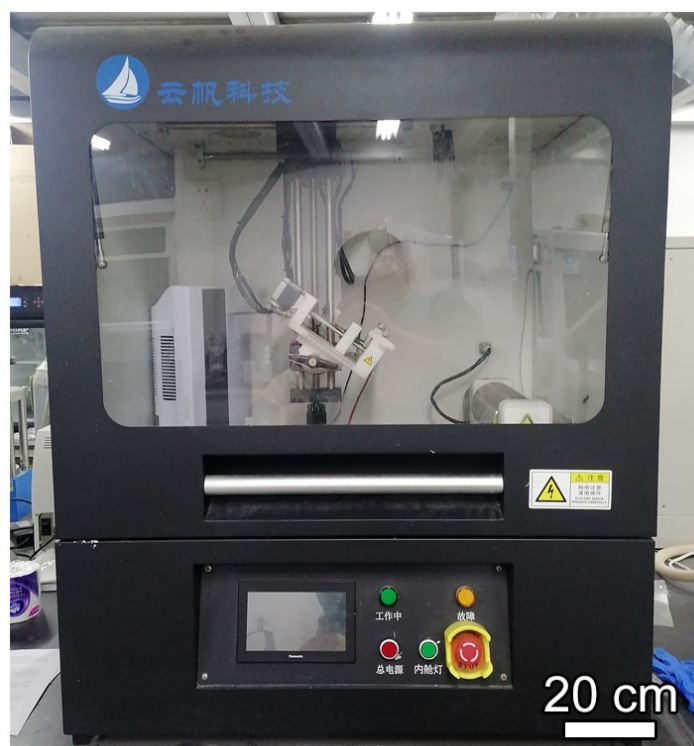


**Figure S20.** A digital image depicting the large-scale electrospaying machine used in this study.

### S3. Supplementary Tables

**Table S1.** Pt contents determined by ICP-OES.

Sample	Pt content (wt.%)
Pt <sub>SA&amp;C</sub> -TiO <sub>2</sub> Janus micromotors	0.22
Pt <sub>NPs</sub> -TiO <sub>2</sub> Janus micromotors	0.24

**Table S2.** Comparison of speed with other reported tubular micromotors.

Name	H <sub>2</sub> O <sub>2</sub> concentration (wt%)	Speed ( $\mu\text{m/s}$ )	Ref
Pt <sub>SA&amp;C</sub> -TiO <sub>2</sub> Janus micromotors	1	113 $\pm$ 47	This work
Pt-ZnIn <sub>2</sub> S <sub>4</sub> micromotors	1	95 $\pm$ 25	15
MOF-based micromotors	1	85 $\pm$ 41	16
Hierarchical hollow $\alpha$ -Fe <sub>2</sub> O <sub>3</sub> /ZnFe <sub>2</sub> O <sub>4</sub> /Mn <sub>2</sub> O <sub>3</sub> Janus micromotors	1	58.1 $\pm$ 8	17
MnO <sub>2</sub> -based microreactors	1	39	18
Bioinspired tubular micromotors	1	29	19
Two-dimensional TiO <sub>2</sub> plate micromotors	1	24 $\pm$ 5	20
3D hierarchical tubular micromotors	1	23	21
A near-infrared light-responsive upconversion nanoparticle micromotor	1	16 $\pm$ 1	22
S-CuFC/Ni/Pt Janus micromotor	5	35.4 $\pm$ 14.3	23
Poly (ETPTA)/Fe <sub>3</sub> O <sub>4</sub> /MnO <sub>2</sub> micromotors	5	29 $\pm$ 6	24

---

## S4. Supplementary Videos

**Video S1.** Bubble-propelled motion of Pt<sub>SA&C</sub>-TiO<sub>2</sub> Janus micromotors in different H<sub>2</sub>O<sub>2</sub> concentrations + 1 wt% SDS.

**Video S2.** Bubble-propelled motion of Pt<sub>NPs</sub>-TiO<sub>2</sub> Janus micromotors in 1 wt% H<sub>2</sub>O<sub>2</sub> + 1 wt% SDS.

**Video S3.** The motion state of Pt<sub>SA&C</sub>-TiO<sub>2</sub> Janus micromotors before and after adding 5 wt% H<sub>2</sub>O<sub>2</sub> + 1 wt% SDS.

**Video S4.** Bubble-propelled motion of Pt<sub>SA&C</sub>-TiO<sub>2</sub> Janus micromotors and Pt<sub>NPs</sub>-TiO<sub>2</sub> Janus micromotors in 1 wt% H<sub>2</sub>O<sub>2</sub> without SDS.

**Video S5.** Motion behavior of Pt<sub>SA&C</sub>-TiO<sub>2</sub> Janus microspheres in 1 wt% H<sub>2</sub>O<sub>2</sub> + 1 wt% SDS.

**Video S6.** Motion behavior of Pt<sub>SA&C</sub>-TiO<sub>2</sub> Janus micromotors in simulated polluted water.

**Video S7.** Bubble-propelled motion of large-scale Pt<sub>SA&C</sub>-TiO<sub>2</sub> Janus micromotors in 1 wt% H<sub>2</sub>O<sub>2</sub> + 1 wt% SDS.

---

## Reference.

1. H. Kim, J. Kim, H. Yang, J. Suh, T. Kim, B. Han, S. Kim, D. S. Kim, P. V. Pikhitsa and M. Choi, Parallel patterning of nanoparticles via electrodynamic focusing of charged aerosols, *Nat. Nanotechnol.*, 2006, **1**, 117-121.
2. A. Jaworek and A. T. Sobczyk, Electro spraying route to nanotechnology: An overview, *J. Electrostat.*, 2008, **66**, 197-219.
3. P. K. Notz and O. A. Basaran, Dynamics of drop formation in an electric field, *J. Colloid Interface Sci.*, 1999, **213**, 218-237.
4. B. Vonnegut and R. L. Neubauer, Production of monodisperse liquid particles by electrical atomization, *J. Colloid Sci.*, 1952, **7**, 616-622.
5. C. D. Hendricks, Charged droplet experiments, *J. Colloid Sci.*, 1962, **17**, 249-259.
6. D. Duft, T. Achtzehn, R. Müller, B. A. Huber and T. Leisner, Rayleigh jets from levitated microdroplets, *Nature*, 2003, **421**, 128.
7. L. Rayleigh, XX. On the equilibrium of liquid conducting masses charged with electricity, *Phil. Mag.*, 1882, **14**, 184-186.
8. W. Liu, J. Midya, M. Kappl, H.-J. Butt and A. Nikoubashman, Segregation in Drying Binary Colloidal Droplets, *ACS Nano*, 2019, **13**, 4972-4979.
9. I. Langmuir, The Evaporation of Small Spheres, *Physical Review*, 1918, **12**, 368-370.
10. B. Cichocki and B. U. Felderhof, Long - time self - diffusion coefficient and zero - frequency viscosity of dilute suspensions of spherical Brownian particles, *The Journal of Chemical Physics*, 1988, **89**, 3705-3709.
11. A. Einstein, Eine neue bestimmung der moleküldimensionen, *Annalen der Physik*, 1906, **324**, 289-306.
12. A. Einstein, Berichtigung zu meiner arbeit: "Eine neue bestimmung der moleküldimensionen", *Annalen der Physik*, 1911, **339**, 591-592.
13. W. Liu, M. Kappl and H.-J. Butt, Tuning the porosity of supraparticles, *ACS Nano*, 2019, **13**, 13949-13956.
14. J. H. Moon, G.-R. Yi, S.-M. Yang, D. J. Pine and S. B. Park, Electro spray-assisted fabrication of uniform photonic balls, *Adv. Mater.*, 2004, **16**, 605-609.
15. M. Yuan, M. Gong, H. Huang, Y. Zhao, Y. Ying and S. Wang, Bubble-propelled plasmon-reinforced Pt-ZnIn<sub>2</sub>S<sub>4</sub> micromotors for stirring-free photocatalytic water purification, *Inorganic Chemistry Frontiers*, 2022, **9**, 5725-5734.
16. H. Huang, J. Li, M. Yuan, H. Yang, Y. Zhao, Y. Ying and S. Wang, Large-scale self-assembly of MOFs colloidosomes for bubble-propelled micromotors and stirring-free environmental remediation, *Angew. Chem. Int. Ed.*, 2022, **61**, e202211163.
17. W. Yang, C. Xu, Y. Lyu, Z. Lan, J. Li and D. H. L. Ng, Hierarchical hollow  $\alpha$ -Fe<sub>2</sub>O<sub>3</sub>/ZnFe<sub>2</sub>O<sub>4</sub>/Mn<sub>2</sub>O<sub>3</sub> Janus micromotors as dynamic and efficient microcleaners for enhanced photo-Fenton elimination of organic pollutants, *Chemosphere*, 2023, **338**, 139530.
18. Y. Yang, K. Hu, Z.-S. Zhu, Y. Yao, P. Zhang, P. Zhou, P. Huo, X. Duan, H. Sun and S. Wang, Catalytic pollutant upgrading to dual-asymmetric MnO<sub>2</sub>@polymer nanotubes as self-propelled and controlled micromotors for H<sub>2</sub>O<sub>2</sub> decomposition, *Small Methods*, 2023, **7**, 2300588.
19. K. Wang, E. Ma, H. Cui, Z. Hu and H. Wang, Bioinspired self-propelled micromotors with improved transport efficiency in the subsurface environment for soil decontamination, *Adv. Funct. Mater.*, 2023, **33**, 2307632.
20. Y. Wang, Z. Li, A. A. Solovev, G. Huang and Y. Mei, Light-controlled two-dimensional TiO<sub>2</sub> plate micromotors, *RSC Advances*, 2019, **9**, 29433-29439.
21. X. Bing, X. Zhang, J. Li, D. H. L. Ng, W. Yang and J. Yang, 3D hierarchical tubular micromotors with highly selective recognition and capture for antibiotics, *J. Mater. Chem. A*, 2020, **8**, 2809-2819.
22. H. Kim and S.-Y. Lee, A near-infrared light-responsive upconversion nanoparticle micromotor propelled by oxygen bubbles, *Chem. Commun.*, 2021, **57**, 512-515.
23. J. Hwang, H.-M. Yang, K.-W. Lee, Y.-I. Jung, K. J. Lee and C. W. Park, A remotely steerable Janus micromotor adsorbent for the active remediation of Cs-contaminated water, *Journal of Hazardous Materials*, 2019, **369**, 416-422.
24. M. Ren, W. Guo, H. Guo and X. Ren, Microfluidic fabrication of bubble-propelled micromotors for wastewater treatment, *ACS Appl. Mater. Interfaces*, 2019, **11**, 22761-22767.